

In Vivo Synthesis of Metabolically Degradable π -Conjugated Conductive Polymers Enabling Seamless Neural Interface Integration and Tissue Repair

Yinhua Qin, Xiaohang Qu, Boyue Huang, Dayu Sun, Haiyan Yin, Ming Ke, Ting Gao, Yuhang Liu, Ju Tan, Gang Li, Xunyi Guo, Youqian Xu,* and Chuhong Zhu*

The seamless integration of bioelectronics with neural tissues is essential for regulating biological signal transmission and understanding complex physiological functions. However, conventional bioelectronic materials face significant limitations, including poor interfacial integration at the cellular level and a lack of controlled degradation, which hinders effective signal transduction and long-term biocompatibility. To address these challenges, a metabolically degradable π -conjugated conductive polymer, poly(pyrrrole-3-carboxylic acid) (PPyCA) is developed and synthesized enzymatically under physiological conditions. The electron withdrawing group, carboxylic acids, reduced the electron cloud density of the pyrrole ring, enhancing the pyrrole ring affinity toward superoxide anion and thereby promoting controlled degradation. The resulting hydrophilic PPyCA has strong tissue affinity, forms seamless bioelectronic interfaces, and undergoes complete metabolic degradation within months. In vivo studies have demonstrated that enzymatically synthesized PPyCA microvesicles (MVs) not only facilitate neural signal transmission but also promote nerve regeneration following injury. Mechanistic investigations revealed that PPyCA upregulates c-FOS and related gene expression through the MAPK pathway, further supporting its role in nerve repair. Importantly, proteomic and metabolomic analyses confirmed the absence of cytotoxic effects. This study establishes a new paradigm for metabolizable electroactive polymers that enable seamless bioelectronic communication and programmed degradation, offering significant potential for biomedical applications.

1. Introduction

The seamless integration of next-generation electronic devices with biological systems represents a revolutionary transformation in the realm of innovative medical treatments.^[1] This integration requires interface materials that coexist harmoniously with biological entities, possess excellent interfacial conductivity between electronic materials and biological tissue for efficient signal transmission, and have tissue repair potential to actively aid in damaged tissue restoration.^[2] Importantly, imparting metabolic degradation capabilities to future electronics enables them to disintegrate within a set period under a dynamic physiological environment, thus eliminating the need for surgical removal from patients and reducing the risk of potential infections.^[3] In the context of interfacial conductivity, the repair and recording of neural tissue hinge critically upon seamless matching of the electrical and mechanical characteristics of the implanted devices with those of the native nervous system. Over the past few decades, notable achievements have been made in leveraging dielectric materials, including

Y. Qin, X. Qu, B. Huang, D. Sun, H. Yin, M. Ke, T. Gao, Y. Liu, J. Tan, G. Li, X. Guo, Y. Xu, C. Zhu
Department of Anatomy
Third Military Medical University
Chongqing 400038, P. R. China
E-mail: yqxu@tmmu.edu.cn; zhuch99@tmmu.edu.cn

Y. Qin, X. Qu, B. Huang, D. Sun, H. Yin, M. Ke, Y. Liu, J. Tan, G. Li, X. Guo, Y. Xu, C. Zhu
Engineering Research Center of the Ministry of Education for Tissue and Organ Regeneration and Manufacturing
Chongqing 400038, P. R. China

B. Huang, D. Sun
Chongqing Medical University
Chongqing 400038, China

T. Gao
Southwest University
Chongqing 400038, China

C. Zhu
State Key Laboratory of Trauma and Chemical Poisoning
Chongqing 400038, P. R. China

 The ORCID identification number(s) for the author(s) of this article can be found under <https://doi.org/10.1002/adfm.202501813>

DOI: 10.1002/adfm.202501813

metals, inorganic semiconductors, and organic semiconductors, for high-quality signal acquisition via implantation.^[4] However, the implantation of exogenous materials invariably triggers a complex tissue response.^[5] This response is typified by alterations in the vasculature and neuropil architecture, accompanied by the onset of inflammation.^[6] During *in vivo* implantation, the inflammatory reaction results in a multitude of unpredictable and erroneous biological signals, which can severely compromise the reliability of the acquired data. In recent years, the *in vivo* fabrication of organic bioelectronic devices induced by biological metabolites has attracted significant attention.^[7] Nevertheless, effective strategies for therapeutic applications and the realization of seamless integration at the cellular level remain to be explored. Therefore, the development of biocompatible and degradable conductive or semiconductor materials for restorative neural interfaces still faces significant challenges.

π -Conjugated polymers hold great promise for facilitating bioelectronic transmission in biological systems because of their tunable responsiveness, biocompatibility, and mechanical flexibility.^[3b,8] These versatile polymers intrinsically modulate the transition between ionic flow and electronic conduction, reducing the electrochemical impedance at the critical interface between electronic devices and living tissues.^[9] Considerable endeavors have been made to integrate π -conjugated polymers into tissue systems, including electrochemical polymerization and genetically targeted chemical assembly on living cells.^[10] To reduce the interfacial impedance between electronic interfaces and plasma membranes, various strategies, such as physical adsorption, covalent bonding, and biodopants, have been developed to create functionalized interfaces.^[11] Nevertheless, the mismatch between static electronics and the dynamic living microenvironment during complex tissue repair presents a significant challenge to achieving seamless integration.

By capitalizing on the intrinsic regenerative potential within the body, a living compartmental bioreactor spontaneously arises from the dynamic physicochemical microenvironment at the injury site, facilitating the synthesis and assembly of π -conjugated polymers.^[12] Under normal conditions, reactive oxygen species (ROS) production and elimination are balanced. The implantation of exogenous materials or the infliction of injury upon tissue leads to an increase in the level of ROS, with hydrogen peroxide (H_2O_2) serving as a typical example.^[13] To regulate regeneration, cells have developed a series of antioxidant enzymes, such as catalase (CAT), for ROS scavenging.^[14] This microenvironment is capable of serving as a living compartmental bioreactor to initiate the *in vivo* polymerization of π -conjugated polymers.

Imparting metabolizable degradability may prevent space occupation and chronic inflammation induced by electronics. However, the availability of degradable conducting and semiconducting materials remains constrained. Currently, the focus of degradable π -conjugated polymers is mainly on modifying degradable polymers such as polylactide and collagen by incorporating them into the polymer backbone or side chains. Prototypical degradable conductive polymers are based on derivatives of polyaniline (PANI), polypyrrole (PPy), and poly(3,4-ethylenedioxythiophene) (PEDOT).^[15] Another strategy for synthesizing degradable π -conjugated polymers involves the incorporation of labile linkages within the polymer backbone.^[16] Nevertheless, degradation products (DPs), specifically nondegrad-

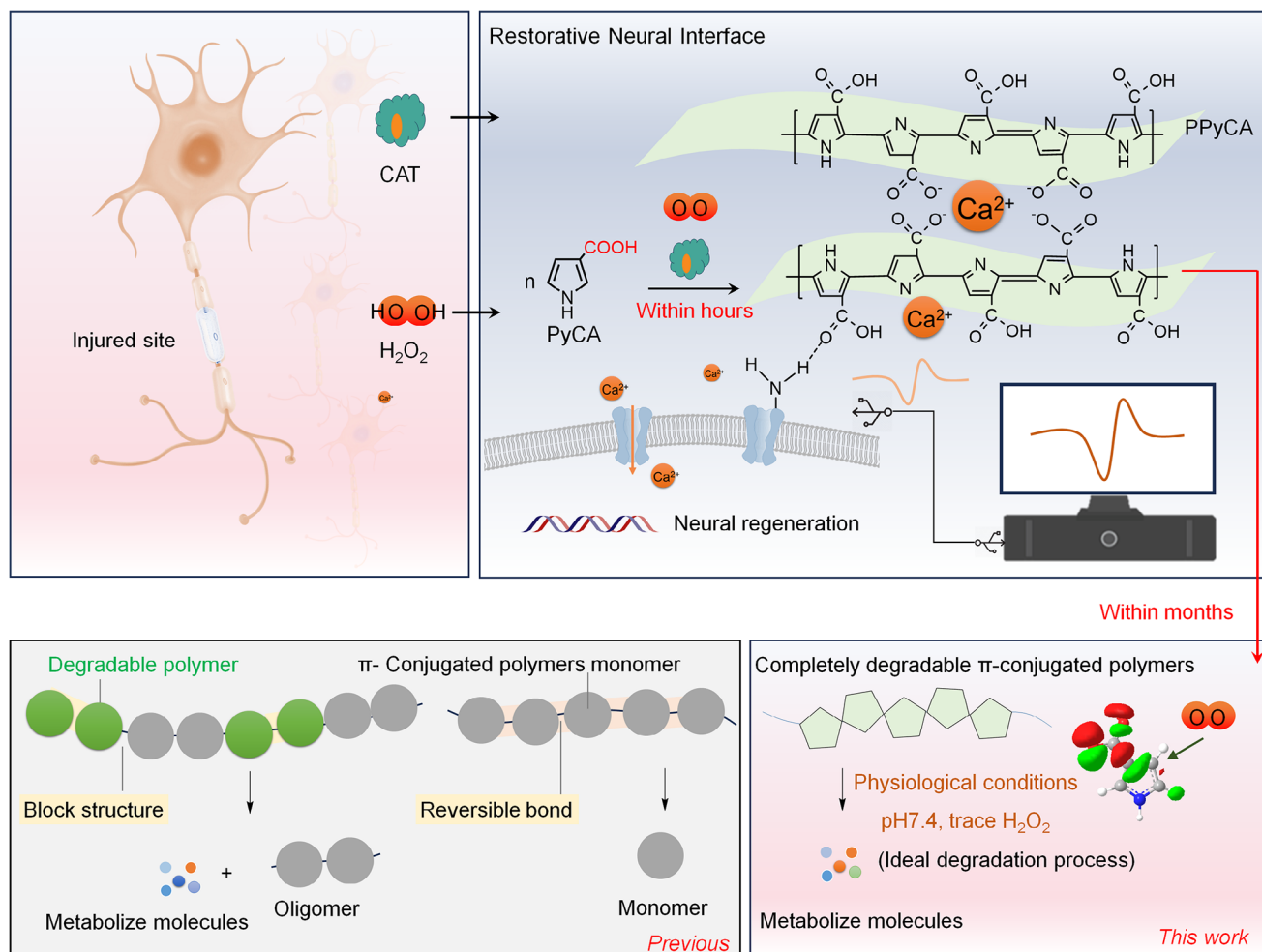
able π -conjugated oligomers or monomers, pose unpredictable risks for biological toxicity, especially within dynamic living organisms.^[17] Moreover, synthetic coupling strategies are constrained by metabolizable degradation mechanisms; for example, imine-based polymers can be readily depolymerized under acidic conditions, but this process is difficult to achieve in a physiological environment.^[18] To advance the design of degradable π -conjugated polymers, diverse factors, such as a limited range of monomer options, mild polymerization conditions, and metabolizable degradation pathways, must be considered. The next generation of organic electronics aims to achieve seamless interfacial communication and programmed or on-demand degradation. Consequently, the development of π -conjugated polymers with designed monomer architectures and metabolizable degradation mechanisms remains a significant challenge.

In this study, pyrrole-3-carboxylic acid (PyCA) was selected as the monomer for the synthesis of π -conjugated polymers. The presence of a carboxyl group within the molecular structure decreases the electron cloud density encircling the pyrrole ring. This property endows the π -conjugated polymers with the ability to undergo degradation, which is facilitated by electron donation from reactive oxygen species (ROS) under physiological conditions. The resulting carboxylated π -conjugated polymer, namely, poly(pyrrole-3-carboxylic acid) (PPyCA), exhibited efficient signal propagation characteristics and degradable properties under simulated physiological conditions. The monomer was introduced into the site of crush injury within the sciatic nerve. *In vivo*, enzymatically synthesized conjugated polymers not only increase signal transmission within damaged nerves but also promote nerve reconstruction (**Scheme 1**). Notably, PPyCA has the capacity for metabolic degradation under physiological conditions after nerve repair. Therefore, this study has developed a metabolizable π -conjugated conductive polymer capable of enzymatic polymerization in living systems, thus paving the way for creating seamless interfaces and programmed metabolizable degradation in various organism applications.

2. Results and Discussions

2.1. Enzymatic Polymerization of the π -Conjugated Polymer

The monomer structure of PyCA was verified by 1H NMR (Figure S1, Supporting Information). 1H NMR (DMSO- d_6): δ = 11.60 (s, 1H, NH), 11.28 (s, 1H, COOH), 7.30 (m, 1H, CH), 6.74 (q, 1H, CH), 6.35 (q, 3H, CH). *In vitro*, the enzymatic polymerization of PPy and PPyCA was initiated by CAT and H_2O_2 (**Figure 1a**; **Figure S2**, Supporting Information). Notably, CAT, a class of oxidoreductases, plays a crucial role in the metabolism of living organisms. The polymerization processes were recorded via digital photography and UV-vis spectroscopy. When both CAT and H_2O_2 were present, the solution turned green, indicating that the polymerization of PPyCA was similar to that of PPy. The evident absorption peak at 480 nm in the UV/Vis spectrum of PPyCA is different from that of PPy at 465 nm. Unlike granules of hydrophobic PPy, scanning electron microscopy (SEM) of PPyCA revealed smaller particles that contributed to improved dispersibility of the interfacial carboxyl groups (**Figure 1b**; **Figure S3**, Supporting Information). The FT-IR spectrum at 1710 cm^{-1} was attributed to the carbonyl group from PPyCA (**Figure 1c**). We measured the



Scheme 1. In vivo, enzymatically synthesized π -conjugated polymers can not only increase signal transmission in damaged nerves but also promote nerve repair. Unlike conventional degradable conductive polymers, PPyCA can be completely degraded under physiological conditions within a few months after tissue repair.

polymer resistance via the four-electrode method and found that PPy had a conductivity of $3.20 \times 10^{-1} \text{ S cm}^{-1}$ and that PPyCA had a much lower conductivity of $1.96 \times 10^{-4} \text{ S cm}^{-1}$ (Figure 1d). The decrease in electrical conductivity is primarily attributed to the reduced dissociation capacity of doped ions in conductive polymers induced by carboxyl functional groups.

2.2. Degradability of π -Conjugated Conductive Polymers In Vitro

To investigate the degradability of PPyCA, the time-dependent degradation under different conditions was recorded (Figure 2a). Without H_2O_2 , PPyCA in PBS scarcely changed throughout the observation period. However, upon the addition of H_2O_2 , the PPyCA solution gradually brightened, with more pronounced results at higher H_2O_2 concentrations. Specifically, an aqueous PPyCA solution at pH 7.4 treated with 5 mM H_2O_2 faded on day 15 and became nearly transparent by day 30, whereas the solution treated with 1 mM H_2O_2 degraded more slowly. The results demonstrated that, in vivo, the H_2O_2 concentration-

dependent degradation reaction occurred very slowly, which was conducive to the maintenance of internal structural function (Figure 2b). Biological tissues metabolize acidic substances, such as lactic acid, in the absence of oxygen during injury, which leads to a reduction in local pH.^[19] PPyCA remains relatively stable in acidic environments, suggesting that conductive polymers can help stabilize and mediate biosignaling during tissue repair. Once tissue healing occurs, the pH returns to normal, and a weakly alkaline environment promotes further polymer degradation. We also recording the degradability of other commercially available conductive polymers, such as PPy, PANI and poly(3,4-ethylenedioxythiophene) poly(styrenesulfonate) (PEDOT:PSS), under the same conditions but did not change until day 30 (Figure S4, Supporting Information). This highlights a key advantage of PPyCA, which exhibits controlled biodegradability, making it more suitable for temporary neural interfaces. The decrease in the absorbance of the characteristic peak confirmed that degradation occurred in solution (Figure S5, Supporting Information). The characteristic spectral changes of PPy were attributed

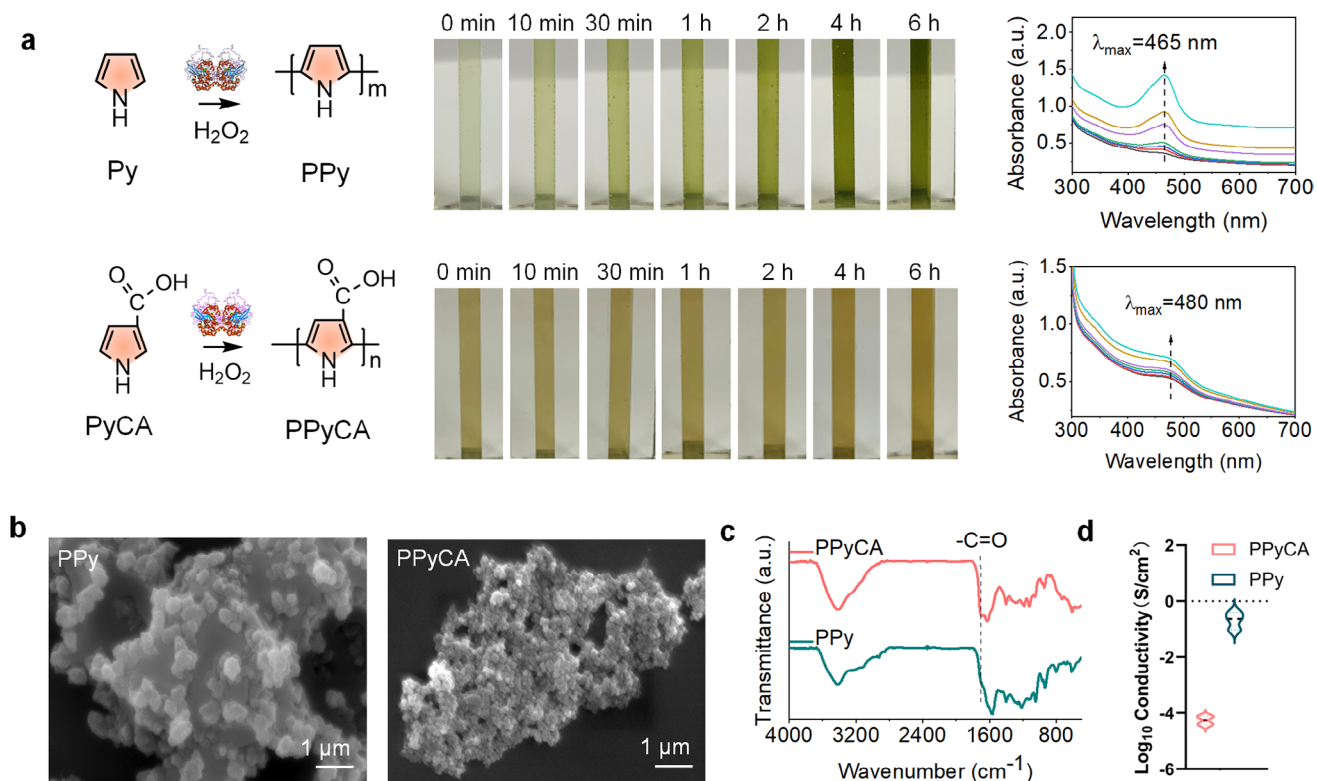


Figure 1. Enzymatic polymerization of a π -conjugated conductive polymer monomer initiated by CAT and H_2O_2 . a) Enzymatic polymerization of PPy and PPyCA was recorded via digital photos and UV-vis spectra. b) SEM images of PPy and PPyCA. c) FT-IR spectra of PPy and PPyCA. d) Conductivity of PPy and PPyCA at 37 °C.

mainly to the oxidation state transformation of the molecular skeleton.

The oxygen anion from H_2O_2 decomposition is more stable in a weakly alkaline environment, which favors the degradation reaction (Figure 2c). This explains why PPyCA is degraded faster at pH 7.4 than at pH 6.5. The surface charge distributions at different pH values illustrate the intrinsic mechanism involved. The oxygen anion is more likely to combine with the backbone of the polymer to initiate the degradation reaction. Liquid chromatography-mass spectrometry (LC-MS) was used to identify the degradation products (Figure 2d; Figure S6, Supporting Information). Despite the complexity of the degradation products, several compounds with different m/z values were detected, helping to elucidate the possible degradation mechanism. The carboxyl groups at the ortho positions reduced the electron cloud density and facilitated the donation of electrons from the oxygen anion, thereby increasing the degradation potential of pyrrole. Moreover, these degradation products exist in trace amounts and can be excreted without long-term body retention.^[20]

2.3. In Vivo Synthesis of Conductive Polymer Microvesicles with Enhanced Cellular Affinity

On the basis of our previous study in which conductive microvesicles were synthesized *in vivo*,^[12] we systematically explored diverse conductive polymer monomers and validated the

microenvironment parameters for *in vivo* synthesis. The potential cytotoxicity of the monomers Py and PyCA was assessed in dorsal root ganglia (DRG) neurons after a 24-h incubation period (Figure 3a,b; Figure S7, Supporting Information). These results suggest that PyCA has better biocompatibility than Py. No reduction in cell viability was observed with the monomer Py at concentrations up to 1 mM, whereas PyCA exhibited remarkable biocompatibility at concentrations up to 5 mM. Biocompatibility is essential for enzymatic polymerization *in vivo*. The low toxicity meets the requirements for the concentration of polymeric monomer. We then employed a sciatic nerve crush injury model as previously described.^[12] When a nerve is injured or damaged, the local tissue responds by recruiting macrophages and undergoing Wallerian degeneration, leading to complex changes in the chemical and biological environment. These dynamic changes persist throughout the repair process. Oxidized dihydroethidium (DHE) was used as a typical indicator of local ROS generation at the injured site (Figure 3c). As part of the feedback mechanism for ROS scavenging, the overexpression of antioxidant enzymes such as CAT satisfies the conditions of oxidative polymerization.

Py and PyCA monomers were injected into the injured sciatic nerves of adult male Sprague-Dawley (SD) rats (Figure 3d). Consequently, the environment at the injury site serves as an ideal dynamic compartmental bioreactor that facilitates PPyCA polymerization. SEM was used to determine the morphology of the PPy and PPyCA polymerizations in the living system

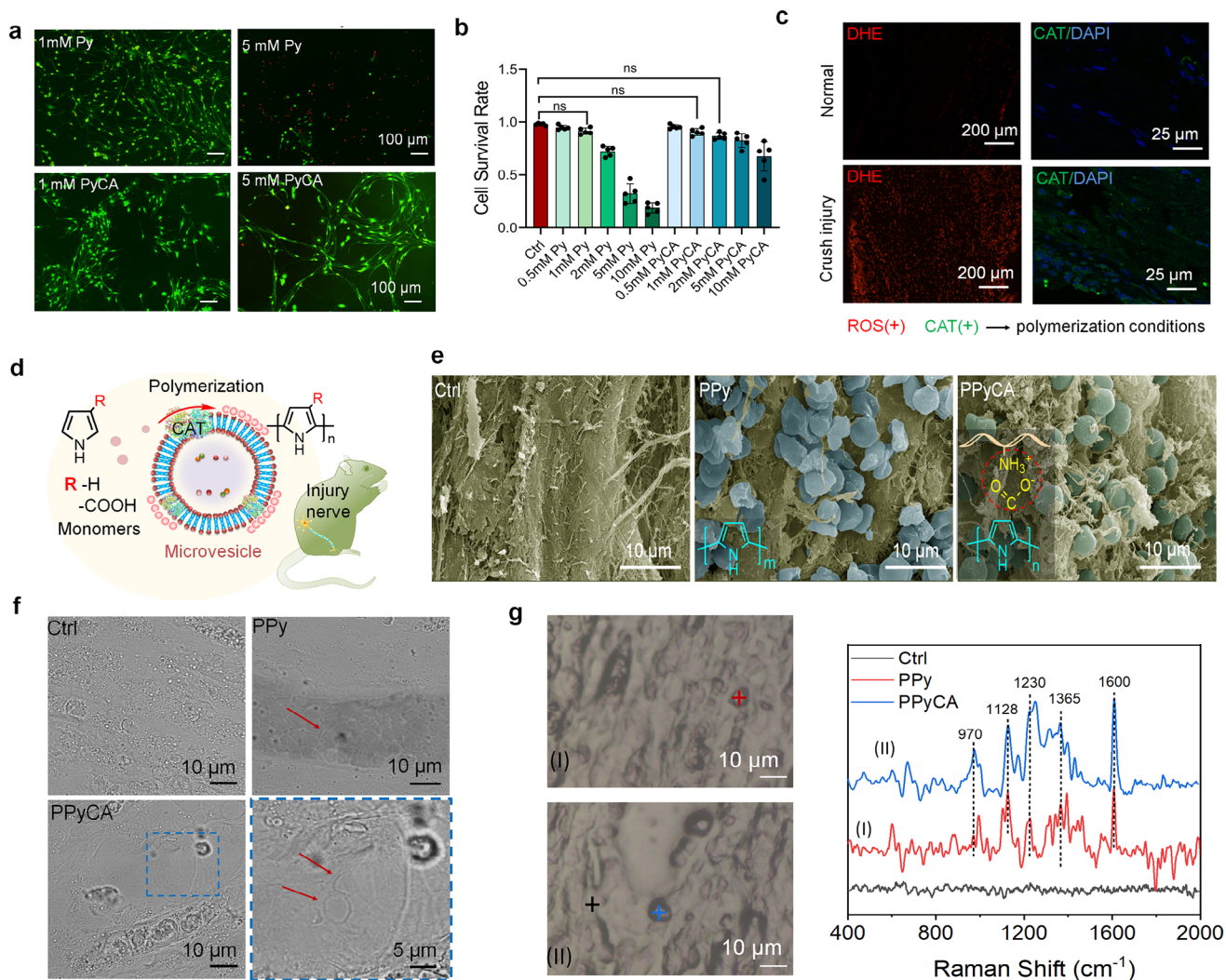


Figure 3. In vivo polymerization of PPy and PPyCA at the injured sciatic nerve site. a) Confocal microscopy analysis of DRG neuronal viability with Py or PPyCA. b) Statistical analysis of cell survival for 24 h. c) Fluorescence imaging showing increased ROS and CAT accumulation at the injury site compared with those at a normal sciatic nerve, creating a suitable microenvironment for Py and PPyCA polymerization. ($n = 3$) d) Schematic illustration of in vivo enzymatic catalysis leading to the formation of PPy and PPyCA microvesicles. e) False-color SEM image of the injured sciatic nerve. f) CLSM bright field images of sciatic nerve sections. g) Laser confocal Raman microspectroscopy analysis of the specified regions in the injured sciatic nerve tissue. ($n = 6$ per group; ns, not significant).

group, potentially contributing to more seamless interfaces between MVs and cells. This finding contrasts with the opposite of the electrical conductivity of the material synthesized in vitro and demonstrates that interfacial connections play a significant role in biological signal transmission. Additionally, changes in neuromuscular compound action potential (CMAP) were recorded. The CMAP amplitude significantly improved on day 4 (Figure 4c, $p < 0.001$).

We then fabricated microelectrode chips to evaluate the ability of the biosignal to record nerve tissue (Figure 4d,e; Figure S10, Supporting Information). The cyclic voltammetry curve showed oxidation peaks at 1.25 V and 1.6 V for PPyCA and at 1.7 V for PPy, which indicates that PPyCA is more prone to redox processes and catalytic activity, facilitating electron or ions transfer, and increasing the sensitivity of biological interfaces (Figure 4f). Interestingly, electrochemical impedance spectroscopy indicated that the

conductivity of the PPyCA MVs in tissue was significantly greater than that of the PPy MVs, with calculated values of PPy 2869 Ω and PPyCA 16.7 Ω . This finding contrasts with the in vitro test results (Figure 4g), where PPy had a conductivity of $3.20 \times 10^{-1} \text{ S cm}^{-1}$ and PPyCA had a much lower conductivity of $1.96 \times 10^{-4} \text{ S cm}^{-1}$. This is a significant difference between the results in Figure 1d, which means that hydrophilicity and affinity are important for biological signal recording. The carboxyl groups of PPyCA bind to the amino groups on the tissue surface, thereby reducing the binding of doping ions. The impedance plot of the PPyCA MVs demonstrated a relatively stable range of 10^4 – 10^5 Hz (Figure 4h). In contrast, the resistance of the PPy MVs remained relatively constant from 10^3 to 10^4 Hz. A similar trend was observed in the phase plot (Figure 4i), with the PPy frequency range exhibiting a phase angle close to 0° at a lower frequency.^[23] At a phase angle of 45° , PPyCA exhibits a greater rate of change

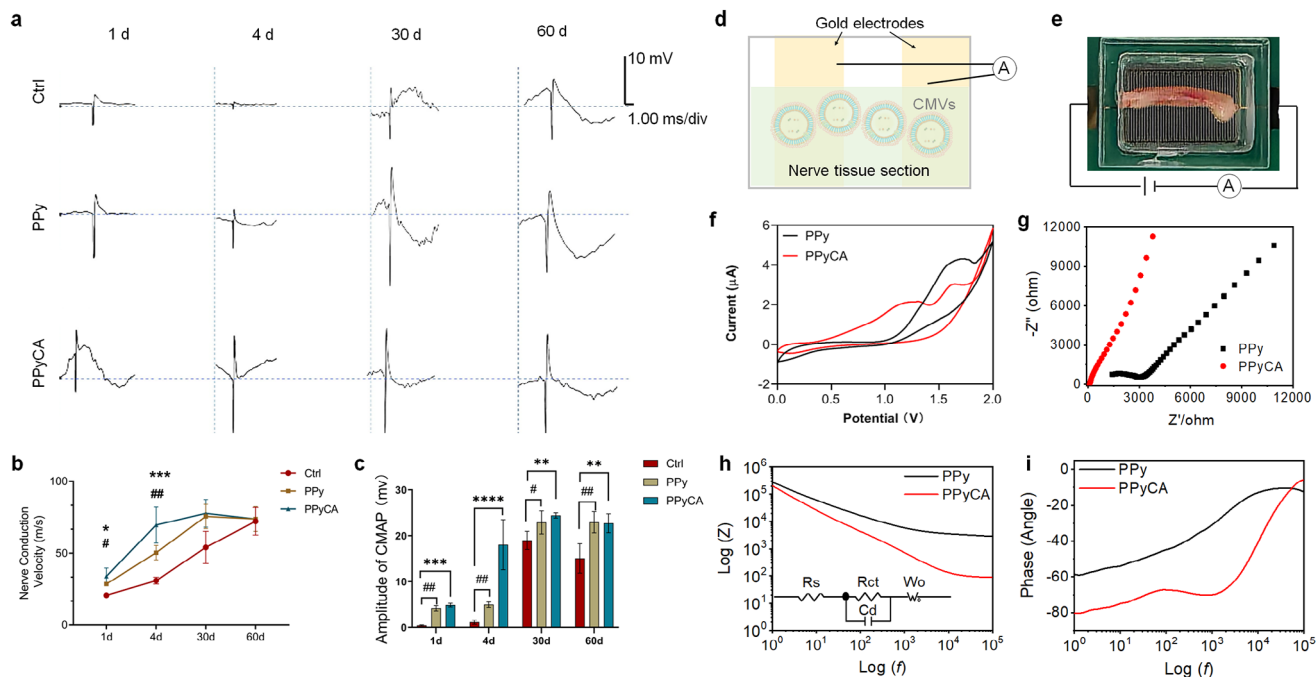


Figure 4. Conductive MVs in situ polymerization promotes nerve conduction. a) Representative curves of nerve trunk compound action potentials obtained via the electrophysiological device after in situ polymerization. b) Statistical motor nerve conduction velocity, and c) CMAP amplitude. d) Schematic of the homemade microelectrode chip used to fix nerve tissue with PPyCA and PPy for conductivity measurements. e) Digital image of nerve tissue on the gold electrode for the electrochemical tests. f) Schematic representation of the microelectrode chip and its digital photo. Biosignal recording of nerve tissue sections: f) Cyclic voltammogram, g) electrochemical impedance spectra, h) impedance plot and inset showing the equivalent circuit, i) platform of the phase angle ($n = 8$ per group). Data are shown as the mean \pm SEM; */#, $P < 0.05$; **/##, $P < 0.01$; ***/###, $P < 0.005$; */, PPyCA versus Ctrl; #, PPy versus Ctrl; (unpaired Student's t-test, one-way ANOVA, two-way ANOVA).

compared to PPy, indicating enhanced ion transfer capability, which is consistent with the previously discussed interfacial affinity. Thus, the MVs formed by the polymerization of PPyCA exhibit a more seamless interface for intercellular signal transmission.

2.5. In Vivo π -Conjugated Conductive Polymer Polymerization Facilitates Nerve Injury Repair

The PPyCA synthesized in situ significantly improved the electrical signal transmission. Next, we investigated whether in situ synthesis affects neural regeneration. We found that the expression of β III-tubulin, an important component of microtubules in neurons, was greater in both the PPy and PPyCA groups than in the control group beginning on day 4 (Figure 5a,b; Figure S11, Supporting Information). To further investigate this phenomenon, data-independent acquisition (DIA) proteomic sequencing of the damaged segment of the nerve on day 4 was performed to identify proteins that are uniquely expressed in the damaged segment of the nerve compared with those in the normal sciatic nerve (Figure 5c). In the comparison between the PPyCA group and the Ctrl group, 528 different proteins were identified, while the PPy group presented 489 differential proteins compared with the Ctrl group. Cluster identity was determined by assessing the differentially expressed proteins (Figure 5d). PPyCA has been shown to increase the expression of proteins associated with cell cycle adaptation, including Hdac7,

Slc25a15, Cntrob, Cdk7, Araf, and Pygm, and to promote the overexpression of proteins related to nerve regeneration and axon growth, such as Ppp1r9a, Cep170b, Myh4/13, Atp1b2, and Kctd17. Notably, Neurabin-1, associated with Ppp1r9a, plays a crucial role in the formation of nerve protrusions and is essential for synapse formation and function because it regulates the migration and directional movement of growth cones.^[24] Gene Ontology (GO) functional enrichment analysis was then performed on the differentially expressed proteins between the PPyCA and Ctrl groups (Figure 5e; Figure S12a, Supporting Information). The results indicated that these different proteins are associated mainly with cytoskeletal motor activity, structural molecule activity, and binding functions. Compared with those in normal nerve tissue, these differentially expressed proteins were enriched primarily in KEGG signaling pathways associated with the metabolism of injured nerves (Figure 5f; Figure S12b, Supporting Information). KEGG pathway analysis revealed increased expression of MEK and CREB within the MAPK pathway, key pathways involved in nerve axon regeneration, and extracellular matrix reconstruction (Figure S12c, Supporting Information). PPy also promoted the expression of proteins associated with the cell cycle and regeneration, such as Slc25a15, Glyctk, Ltbp4, and Lama1 (Figure S13a, Supporting Information). Specifically, PPy has been shown to stimulate high expression levels of Celsr2, a protein crucial for various neuronal functions. Celsr2 is vital in regulating ciliogenesis, neuronal migration, axon growth and regeneration, and dendrite development.^[25] Additionally, GO biofunctional

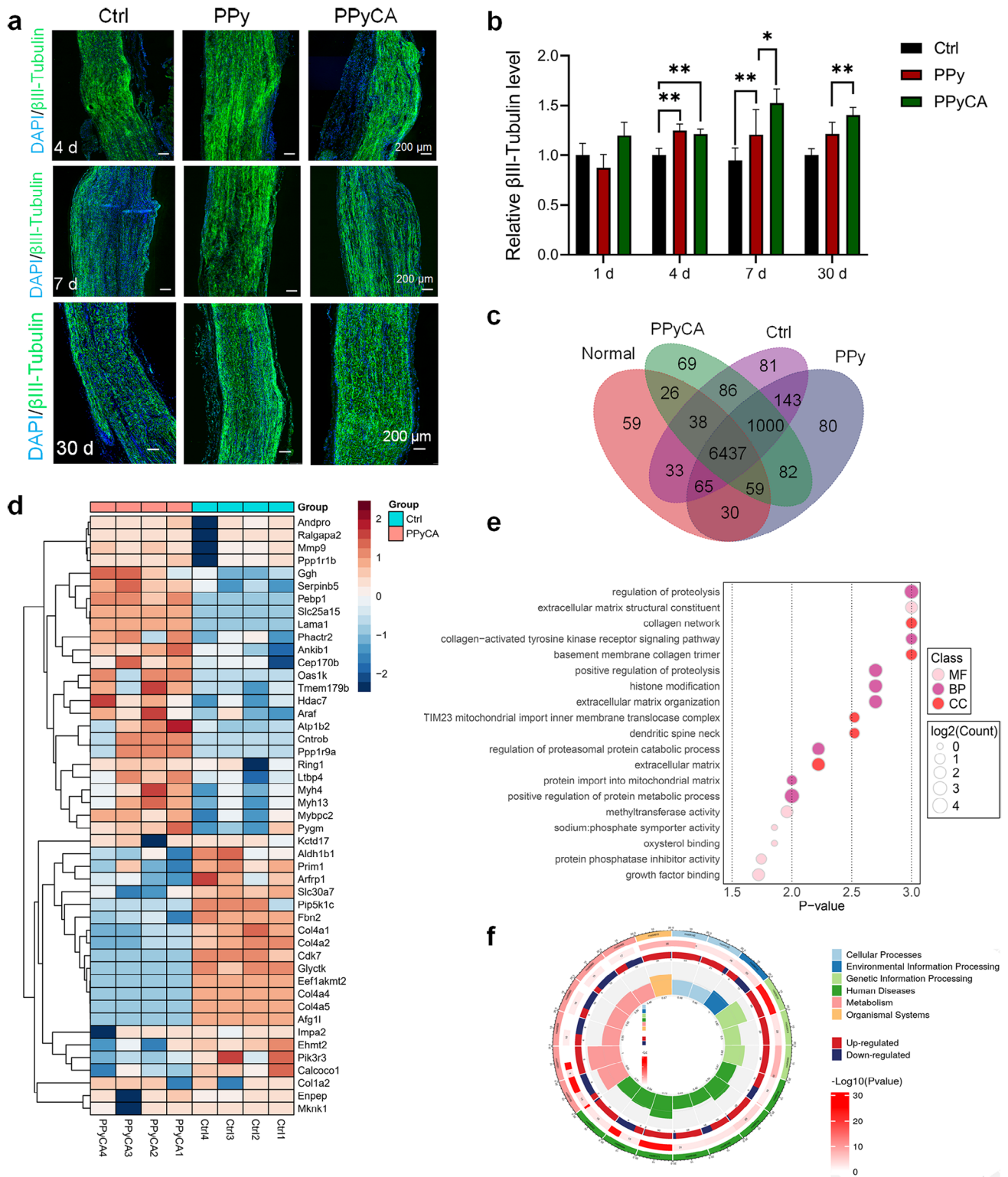


Figure 5. PPyCA endogenously activates neuronal repair. a, b) CLSM images of β III-tubulin-stained nerve tissue and statistical analysis of fluorescence intensity. c) DIA proteomics sequencing was used to determine the unique peptide counts of the normal, Ctrl, PPy, and PPyCA groups. d) Heatmap of cluster identity by differentially expressed proteins in the PPyCA versus Ctrl groups. e) GO functional enrichment analysis was performed on the differential PPyCA versus Ctrl. f) KEGG enrichment analysis between the PPyCA group and the normal group ($n = 8$ per group). The data are shown as the means \pm SEMs; *, $P < 0.05$; **, $P < 0.01$ (unpaired Student's t-test, two-way ANOVA).

enrichment analysis of the differentially expressed proteins revealed their roles in critical processes such as synapse assembly, which is essential for innervation, and calcium cation antiporter activity (Figure S13b, Supporting Information). Although the PPyCA and PPy groups displayed numerous similarities, subsequent KEGG analysis of these different proteins suggested that their differences were mainly concentrated in the biosynthetic pathways of glycosphingolipids and glycosaminoglycans (Figure S13c, Supporting Information). Therefore, both PPy and PPyCA can be synthesized in situ, enhancing neural electrical signal conduction in the short term while rapidly initiating the neural regeneration process and promoting the expression of axon-related proteins.

2.6. PPyCA Promotes c-FOS and Related Gene Expression Through the MAPK Pathway

Next, we utilized PPyCA synthesized by the CAT enzyme in vitro and isolated DRG neurons to verify the related pathways. Fluoro-4 AM (Fluo-4 AM), a fluorescent calcium indicator, was used to monitor intracellular Ca^{2+} activity in isolated DRG neurons. To trigger membrane depolarization, neurons were perfused with a high concentration of potassium chloride (100 mM).^[26] Both PPy and PPyCA significantly facilitated Ca^{2+} influx (Figure 6a, Videos S1–S3, Supporting Information). The fluorescence signals were converted into the $\Delta F/F$ ratio (change in fluorescence from baseline fluorescence) (Figure 6b). PPyCA showed a greater fluorescence response than PPy did, suggesting a more efficient interface for Ca^{2+} influx. This enhanced response is attributed to the greater affinity of the carboxyl groups present in the PPyCA, which may promote more seamless interactions with neuronal cells.

We also further investigated the signaling pathway by which PPy and PPyCA promote regeneration in DRG neurons. The reverse transcription quantitative polymerase chain reaction (RT-qPCR) results revealed that PPyCA activated the ERK/MAPK pathway and induced the expression of genes such as SRF, CREB, and c-FOS (Figure 6c), which was consistent with the proteomics results showing that PPyCA could increase the expression of the Raf and Creb proteins. Western blot analysis revealed that the expression of c-FOS, a functional marker of neuronal activity that is also induced by PPyCA, was significantly different from that induced by PPy (Figure 6d,e; Figure S14, Supporting Information). However, the effect of PPy on the activation of the ERK/MAPK-c-FOS signaling pathway in DRG neurons was less pronounced. Consequently, the expression of additional proteins involved in nerve regeneration was assessed, revealing that PPy enhanced the expression of the Arc protein. Arc is essential for regulating actin cytoskeleton dynamics and synaptic plasticity.^[27] These findings suggest that PPyCA initiates nerve regeneration through the ERK/MAPK-c-FOS pathway, enhancing the activity of proteins such as neurabin-1 and the sodium/potassium-transporting ATPase subunit beta-2, which expedites nerve reconstruction (Figure 6f). Additionally, the upregulation of myosin protein expression by PPyCA facilitated extracellular matrix remodeling and neurite growth.

2.7. Metabolizable Degradation of the PPyCA MVs under Dynamic Physiological Conditions

To examine the long-term presence of PPy and PPyCA synthesized in vivo, we performed additional histological assessments on days 30 and 60 (Figure 7a,b). PPy, as a nondegradable polymer, was observed to be gradually expelled toward the epineurium during nerve repair. This expulsion is consistent with previous findings on nondegradable polyaniline.^[12] Furthermore, on day 60, neural tissue immunolabeled with LYVE1 presented increased formation of lymphatic microtubules in the PPy MVs group. This increase is primarily associated with the discharge of the PPy MVs (Figure 7c,d). Interestingly, on day 60, PPyCA MVs were barely detectable in the outer membrane and edges of nerve tissue, with only trace amounts of MVs observed in nerve tissue on day 30. This biodegradation process occurs under physiological conditions and is highly important for biomedical applications of conductive materials. To confirm and potentially accelerate this degradation process in tissue, we subsequently treated the samples with different pH values and H_2O_2 concentrations (Figure S15, Supporting Information). The results demonstrate that the PPyCA MVs are slowly degraded at pH 7.4 and that the degradation rate increases with increasing H_2O_2 concentration.

The biosafety of DPs is essential for nerve repair. The biosafety of the PPy and PPyCA DPs was assessed after a 24-h incubation with DRG cells. Live/dead staining of DRG neuronal cells revealed no apoptosis, indicating that the DPs of PPy and PPyCA did not cause notable cell death (Figure 8a,b). The impact of DPs on neuronal energy metabolism was evaluated via Agilent Seahorse XFe96 analyzers. The results indicated that PPyCA DPs treated with higher H_2O_2 concentrations did not show an increase in the oxygen consumption rate (OCR), as measured by the Cell Mito Stress Test (Figure 8c,d). Additionally, mitochondrial functional parameters, including basal respiration, ATP-linked respiration, maximal respiration, and spare respiratory capacity, were not adversely affected by DPs. PPy DPs at high (H) and low (L) concentrations, along with PPyCA DPs at low concentrations, positively affected the basal respiratory capacity and ATP production capacity of DRG cells. The results are mainly because polymers that have not undergone degradation still have a conductive function and activate cell function. The fully degraded PPyCA DPs did not affect cell function and proved to be safe in vivo. Proteomic analysis, supported by in vivo synthesis data of PPy and PPyCA, revealed that both polymers increased the expression of proteins related to mitochondrial functions (Figure 5d). These proteins included Slc25a15 and Mtco2, which may have contributed to the observed enhancements in cellular metabolism.

To investigate the long-term metabolic effects of PPyCA degradation under physiological conditions, off-target metabolomics sequencing was conducted on sciatic nerve tissue 60 days after treatment. 3D-Principal component analysis (PCA) revealed that the metabolic signature of the PPyCA group closely resembled that of the normal sciatic nerve (Figure S16, Supporting Information). A detailed comparison of metabolites between the PPyCA and Ctrl groups revealed that most of these metabolites were lipids, lipid-like molecules, and organic acids and their derivatives. In contrast, some metabolites in the PPy group,

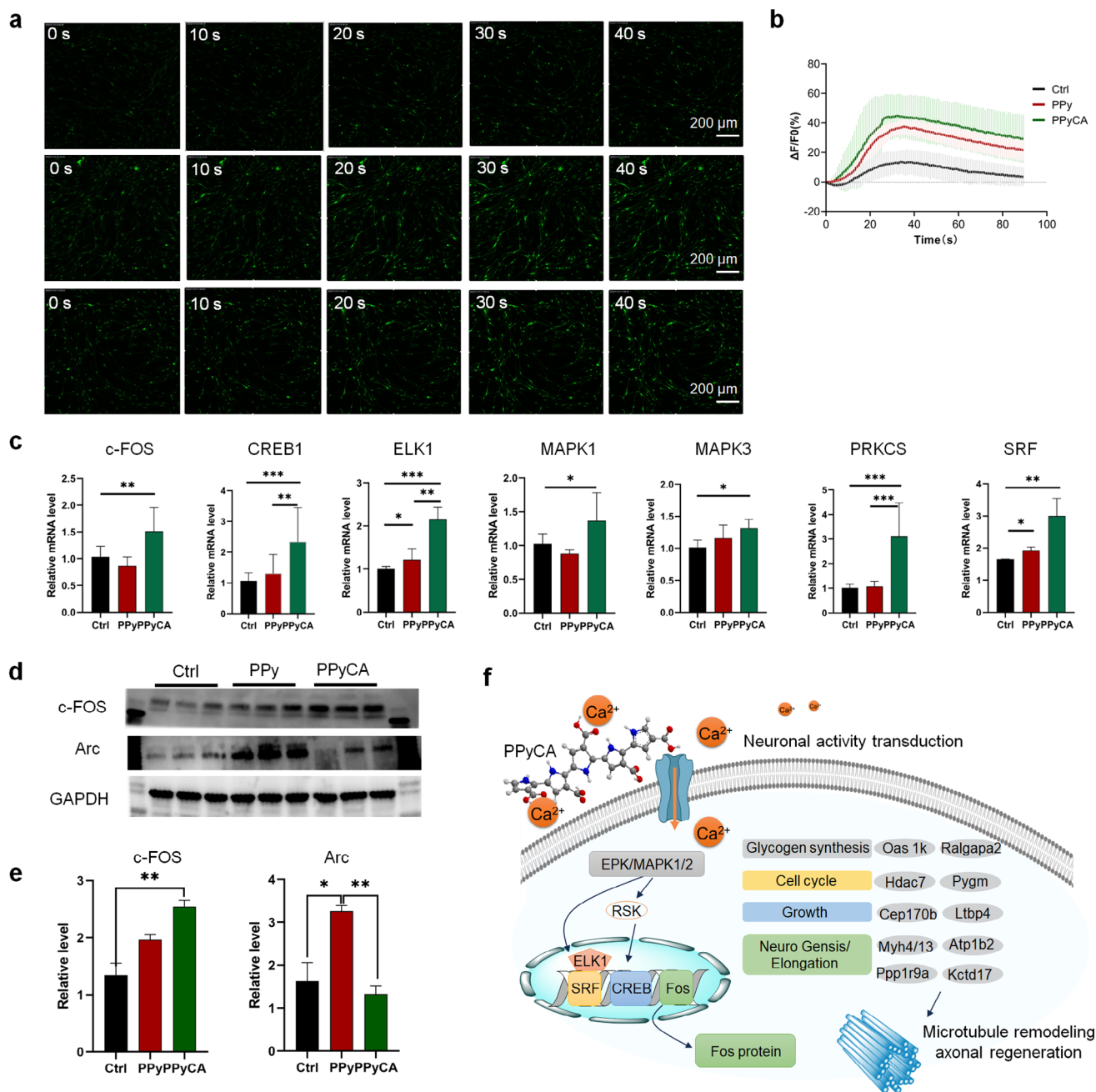


Figure 6. Enhancement of neuronal regeneration pathways by PPyCA. a,b) PPy MVs and PPyCA MVs promoted Ca^{2+} influx in DRG neuronal cells, and Fluo-4 AM was used as a fluorescent probe. c) mRNA expression of c-FOS, CREB1, ELK1, MAPK1, MAPK3, PRKCS, and SRF. d) The protein expression of c-FOS and Arc was measured via Western blotting. e) Changes in relative protein expression. f) PPyCA MVs activate neuronal regeneration via the ERK/MAPK-c-FOS pathway. (mean \pm s.e.m; * $P < 0.05$; ** $P < 0.01$, *** $P < 0.005$).

similar to benzenoids, suggested incomplete degradation (Figure 8e; Figure S17, Supporting Information). Enriched KEGG pathway analysis indicated that the primary focus of the comparative analysis among the PPyCA, PPy, and Ctrl groups was on the synaptic vesicle cycle and cAMP signaling pathway (Figure 8f), which are crucial for neurotransmitter transmission in axons. Compared with those in PPy, the four differentially abundant metabolites in the superclass analysis were associated

with lipid and lipid-like molecules, and the correlation analysis also revealed a positive correlation between PPyCA and these differentially abundant metabolites (Figure 8g,h). Thus, the metabolic analysis revealed that PPyCA can be synthesized and degraded under physiological conditions, with its degradation products exhibiting no long-term biological toxicity to cells or nervous tissue.

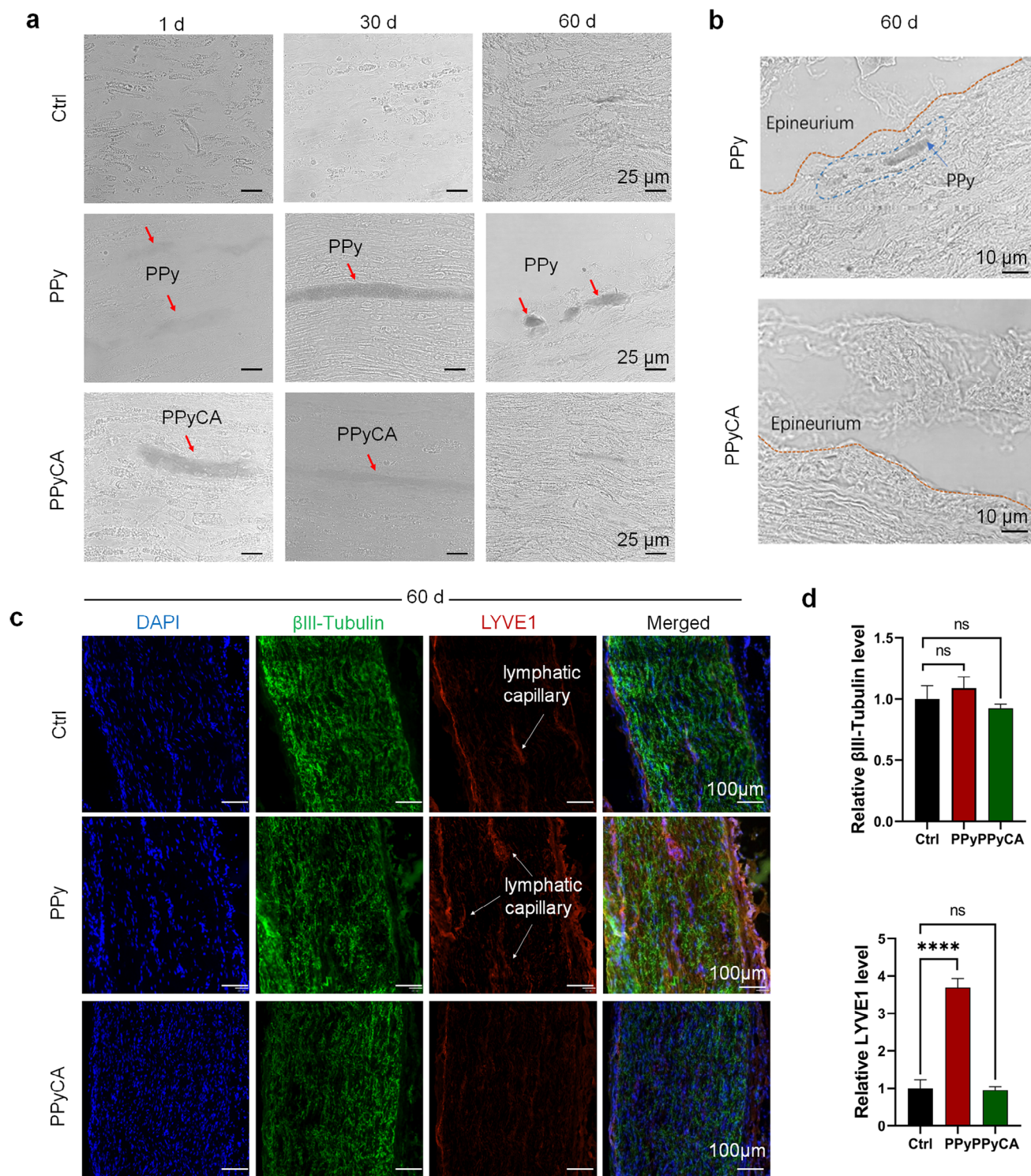


Figure 7. PPy MVs are expelled from the sciatic nerve, and PPyCA MVs are biodegraded in situ during nerve repair. a) CLSM bright-field images of the injured sciatic nerve; red arrows indicate the location of in situ polymerization of the conductive polymer. b) CLSM bright-field images of the neuronal epineurium on day 60. c) Immunofluorescence staining of β III-tubulin and LYVE1 on day 60; white arrows indicate lymphatic capillaries. d) Statistical analysis of the relative β III-tubulin level and relative LYVE1 level. The data are shown as the means \pm SEMs; ns, not significant; **** $P < 0.001$. (unpaired Student's t-test, one-way ANOVA).

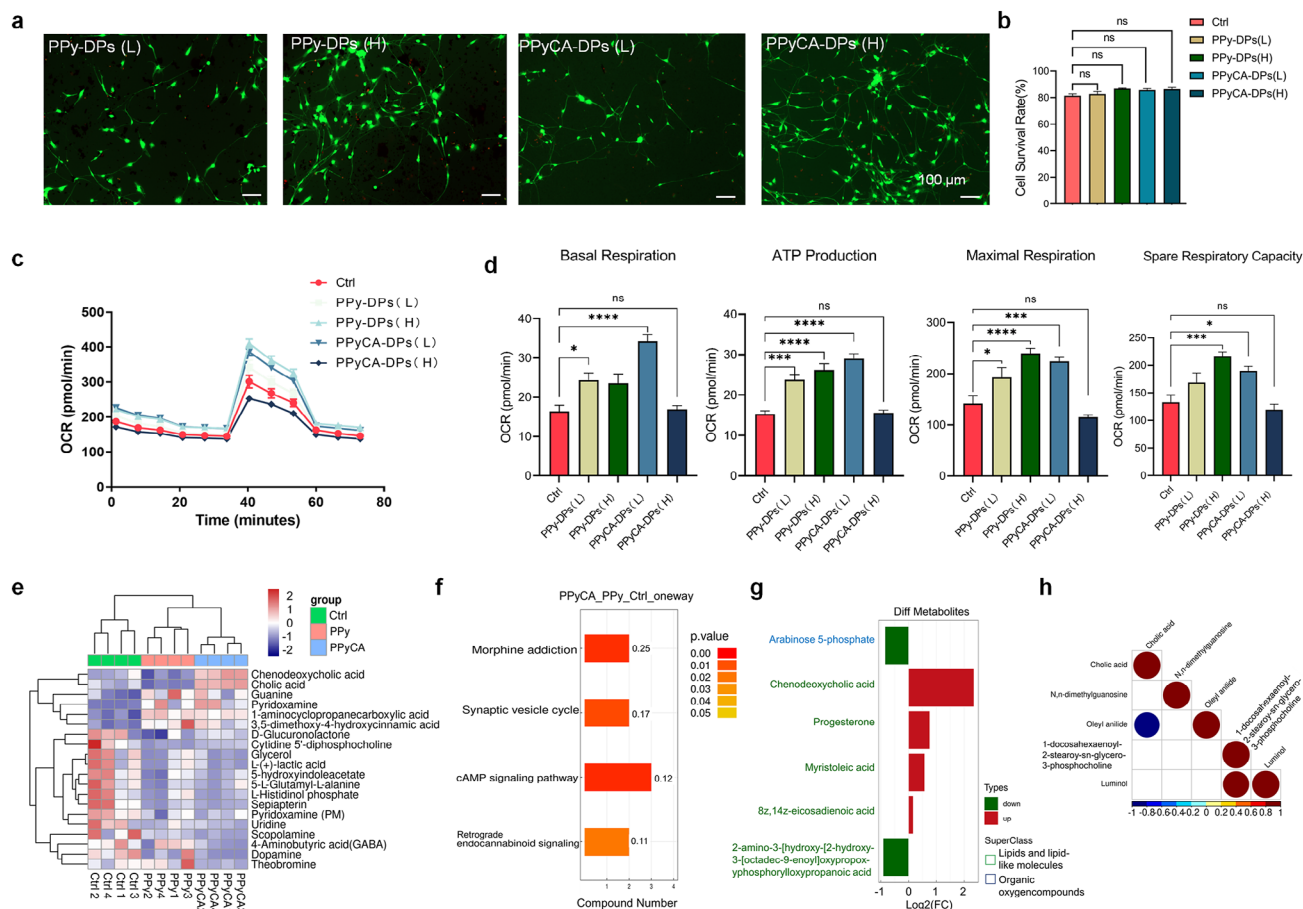


Figure 8. Biosafety of the PPy degradation products. a) Live/dead staining of DRG neuronal cells. The DRG neuronal cells were incubated with DPs of PPy or PPyCA for 24 h. L, 1 mM H₂O₂ treatment; H, 5 mM H₂O₂ treatment. b) Statistical analysis of the cell survival rate after 24 h of incubation with different DPs. c) OCR of DRG cells through the cell Mito Stress Test. d) Statistical analysis of basal respiration, ATP production, maximal respiration, and spare respiratory capacity. e) Heatmap of cluster identity by differentially abundant metabolites comparing PPyCA versus PPy versus Ctrl. f) Enriched KEGG pathways of PPyCA versus PPy versus Ctrl. g) The superclass of differentially abundant metabolites between PPyCA and PPy. h) Correlation analysis between PPyCA and PPy ($n = 8$). The data are shown as the mean \pm SEM; ns, not significant; * $P < 0.05$, *** $P < 0.005$, **** $P < 0.001$. (unpaired Student's *t*-test, one-way ANOVA).

3. Conclusion

In this study, we designed an enzyme-catalyzed π -conjugated conductive polymer, PPyCA, which can facilitate neural repair and biosignal recordings and is capable of complete degradation within a specific period in the physiological environment. By introducing carboxyl groups into the pyrrole ring, the electron cloud density of the polymer chain is effectively decreased, thereby facilitating the binding of oxygen anions and triggering the degradation reaction. In the pathological tissue environment, π -conjugated conductive polymers can be enzymatically synthesized *in vivo* by the endogenous CAT enzyme and H₂O₂. PPyCA effectively enhances the internal flow of biological calcium signals and increases the tissue repair capacity. Concurrently, this conductive interface can significantly reduce the interface impedance, which is beneficial for the accurate recording of biological signals. Following tissue repair, complete degradation can be achieved within a few months, minimizing the risks of space-occupying effects and inflammation. Electrophysiological,

proteomic, and metabolomic analyses confirmed that PPyCA initiates neuronal regeneration pathways and does not pose a long-term risk of biological toxicity. These results are highly important for the development of flexible and seamless bioelectronic interfaces and lay the foundation for research and application in the field of regenerative medicine.

4. Experimental Section

Chemicals: Py and PyCA were purchased from Sigma-Aldrich (USA). Polystyrene sulfonic acid (PSS) and PANI were purchased from Aladdin (CN). PEDOT:PSS was purchased from Merck. 1,2-Dipalmitoyl-sn-glycerol-3-phosphate (DPPA) and 1,2-dipalmitoyl-sn-glycerol-3-phosphocholine (DPPC) were purchased from Avanti. The LIVE/DEAD staining kit was obtained from Proteintech (CN), collagenase I from Solarbio (CN), and Matrigel from Corning (USA). The cell culture media, fetal bovine serum (FBS), B-27, dihydroethidium (DHE), catalase (CAT), Alexa Fluor 488-conjugated goat anti-rabbit secondary antibody, and Alexa Fluor 594-conjugated goat anti-mouse secondary antibody were obtained from

Thermo Fisher Scientific (USA). The primary antibodies utilized in this study were as follows: β III-Tubulin (53–4510–82), LYVE1 (mouse monoclonal antibody, Thermo Fisher Scientific (USA, product # 14-0443-82), catalase (rabbit polyclonal antibody, Proteintech, product # 212601-AP), c-Fos (rabbit polyclonal antibody, Cell Signaling Technology, product # 4384), and Arc (rabbit polyclonal antibody, Cell Signaling Technology, product # 38 916). The Fluo-4 calcium assay kit was obtained from Beyotime (CN, product # S10615). A Seahorse XF Cell Mito Stress Test Kit (product # 103015–100), XF DMEM (product # 103575–100), pyruvate (product # 103578–100), glutamine (product # 103579–100) and 10 mM glucose (product # 103577–100) were obtained from Agilent (USA).

¹H NMR Analysis: For the ¹H NMR of PyCA, PyCA was dissolved in 0.6 mL of DMSO-*d*₆ solution, and the solution was loaded into an NMR tube. The NMR tube was subsequently inserted into the sample chamber and tested with an Agilent DD2-600/54 spectrometer at 600 MHz.

Gel Permeation Chromatography (GPC): GPC was conducted using an Agilent 1260 Infinity II system to analyze the molecular weight distribution of polymerized PPyCA. Separation was performed on an Agilent PL aquagel-OH MIXED-M column at a controlled temperature of 40 °C. An aqueous 0.1 mol L⁻¹ NaNO₃ solution served as the mobile phase, with a flow rate of 1 mL min⁻¹. The injection volume was 20 μ L, and polyethylene glycol (PEG) standards were used for molecular weight calibration.

Four-Point Probe Measurements: 0.1 g CAT enzymatic polymerized PPy/PPyCA sample was spread in a 10 mm diameter mold and compressed at 30 MPa to form a uniform pellet. Conductivity was measured at 3 MPa using an insulation resistance tester (RK2683AN, Shenzhen Meiruike).

Neuronal Cell Isolation: Animal experiments were conducted in accordance with the Laboratory Animal Administration Rules of China and were approved by the Ethics Committee of the Third Military Medical University (AMUWEC20230031). Neuronal cells were isolated from the DRGs of newborn Sprague-Dawley (SD) rats. After decapitation, the DRGs were collected on ice, incubated in Dulbecco's modified Eagle's medium (Gibco) supplemented with 10 mg mL⁻¹ collagenase I, and then cut into pieces. After incubation at 37 °C for 30 min with occasional shaking, the digested DRGs were resuspended in a cell culture medium containing 10% heat-inactivated FBS and filtered through a 70- μ m nylon cell strainer to create a single-cell suspension. This suspension was transferred to a new 1.5 mL tube, followed by two rounds of low-speed centrifugation to remove satellite cells. The neurons were then plated on Matrigel (0.1 mg mL⁻¹)-coated 24-well plates at a density of 8000 cells mL⁻¹ and cultured in a humidified environment at 37 °C with 5% CO₂. The culture medium for the DRG neuronal cells included 96.5% neurobasal medium (Gibco), 2% B-27 supplement (Invitrogen), 1% GlutaMAX (Gibco), and 0.5% antibiotic-antimycotic solution (Gibco).

Cell Culture and Treatment: Primary DRG neurons were cultured for 5 days and then incubated with Py or PyCA monomer (1 mM to 10 mM) for 24 h. After three washes with PBS (pH = 7.4), the cells were stained with a LIVE/DEAD staining kit and observed via a fluorescence microscope (Leica, Evos FL). Image analysis was carried out using ImageJ software (National Institute of Health, Bethesda, MD, USA).

Animal Models and Py or PyCA Injection: Adult male SD rats (200–230 g) were randomly divided into three groups. Under anesthesia, the sciatic nerve of the left hind limb was exposed via a \approx 2 cm skin incision on the posterior thigh. The overlying muscles were bluntly separated to reveal the sciatic nerve. A standardized crush injury was induced using fine forceps, applying constant pressure for 30 s at the mid-thigh level, \approx 5 mm proximal to the nerve bifurcation. The forceps were then gently released, and the site was inspected for morphological changes. Afterward, 10 μ L of either Py or PyCA solution was injected into the crushed area with a 0.3 \times 8 mm² insulin needle (KDL, China). An equal volume of PBS was injected as a control. The animals were then housed individually in cages and kept on a 12/12-h light/dark cycle with ad libitum access to food and water.

Detection of ROS: The level of ROS was detected via a DHE probe. In brief, the freshly collected tissues were immediately sectioned on a cryotome and then incubated with DHE (100 μ M in PBS) for 30 min at 37 °C

in the dark. Images of the samples were captured via a fluorescence microscope (Olympus, VS200).

Immunofluorescence Staining: The sciatic nerves were isolated and fixed at 4 wt.% PFA in PBS. The samples were subsequently transferred to 30 wt.% sucrose, frozen, and embedded in OCT compound. Sagittal or coronal sections, 10 μ m thick, were then prepared from the embedded tissues. Following rinsing with PBS and blocking with goat serum, the sections were incubated with primary antibodies at 4 °C overnight. Alexa Fluor-conjugated goat secondary antibodies were used to facilitate fluorescence imaging, and DAPI was used to stain the cell nuclei. All the sections were observed using CLSM.

Confocal Raman Microscopy: Tissue slices were placed on glass slides, sequentially rinsed with PBS and DI water, and then subjected to freeze-drying. Images were captured using a confocal Raman microscope, specifically a LabRam HR Evolution (Horiba) instrument equipped with a red laser at an excitation wavelength of 632.8 nm.

Electrophysiological Assessment: At specified time intervals, the animals were anesthetized, and the sciatic nerves were exposed for CMAP measurement. Electrical stimuli were applied to the proximal and distal ends of the nerves. The gastrocnemius muscle data were collected using the RM6240 Multichannel Physiological Signal Acquisition System (Chengdu, China). The stimulation parameters were set as follows: stimulation duration, 0.2 ms; stimulation intensity, 10–50 mV; bandpass, 0.1–100 Hz; scanning speed, 1000 ms D⁻¹; and sensitivity, 0.1–2.0 mV D⁻¹.

Electrochemical Tests: A gold microelectrode array was fabricated on a glass substrate using photolithography, with an interelectrode spacing of 100 μ m (Figure S9, Supporting Information). The dissected sciatic nerve tissue was sliced into 100 μ m-thick sections and then transferred onto the electrode surface for further testing on an electrochemical workstation (CHI660E, Shanghai Chenhua, China). CV curves were recorded with a scan rate of 10 mV s⁻¹ and a potential window of 0 to 2.0 V. EIS was tested at a frequency range of 10 Hz–10⁵ MHz and an amplitude of 10 mV. Each sample was measured three times, and the data were averaged.

For quantitative proteomics via data-independent acquisition (DIA), the samples were lysed via SDT lysis buffer (4% SDS, 100 mM Tris-HCl, pH 7.6) for protein extraction, and various extraction methods were employed for different sample types. Protein quantification was performed via the BCA method. For each sample, 15 μ g of protein was mixed with 5 \times loading buffer, boiled, and then subjected to SDS-PAGE (4%–20% gradient gel, 180 V for 45 min), followed by Coomassie Brilliant Blue R-250 staining. All the samples were processed for trypsin digestion via the filter aided proteome preparation (FASP) method. The peptides were desalted via a C18 cartridge, freeze-dried, and reconstituted in 40 μ L of 0.1% formic acid solution. The peptide concentration was determined by measuring the optical density at 280 nm (OD280). The internal reference standard peptide (iRT) was added to each sample. Peptide detection was conducted using Astral high-resolution mass spectrometry in Data-Independent Acquisition (DIA) mode. DIA analysis was performed via the nanoflow Vanquish Neo system (Thermo Fisher Scientific) for chromatographic separation. The samples were analyzed with an Astral high-resolution mass spectrometer (Thermo Scientific) in positive ionization mode, with a precursor ion scan range of 380–980 m/z. The first-stage mass spectrometry resolution was set at 240 000 at 200 m/z, the normalized AGC target was 500%, and the maximum IT was 5 ms. MS2 utilized DIA data acquisition mode with 299 scan windows, an isolation window of 2 m/z, an HCD collision energy of 25 eV, a normalized AGC target of 500%, and a maximum IT of 3 ms. DIA data were processed via DIA-NN software with the following parameter settings: trypsin was used as an enzyme, the maximum number of missed cleavage sites was set to 1, carbamidomethyl (C) was set as a fixed modification, and oxidation (M) and acetyl (protein N-term) were set as dynamic modifications. Proteins identified from the database search had to pass the set filtering parameter of FDR < 1%.

RT-qPCR: Gene expression levels were assessed by evaluating relative mRNA expression via a qPCR system (Bio-Rad). After being cultured for 14 days, total RNA was isolated via TRIzol reagent (Invitrogen, CA, USA) and reverse-transcribed via the PrimeScript RT Reagent Kit (Takara Shuzo Co., Kusatsu, Shiga, Japan), both of which were performed according to

the manufacturers' instructions. The sequences of the primers used for the qPCR measurements are listed in Table S1 (Supporting Information).

Western Blotting Assay: A routine procedure was used for Western blotting. Primary antibodies, including rabbit anti-rat CaM, anti-CaN, anti-NFAT, and anti-GAPDH (Abcam, UK), were incubated with the immunoblotted proteins for 12 h at 4 °C. Following five washes with Tris-buffered saline containing Tween-20 (TBST), the immunoblotted proteins were incubated with horseradish peroxidase (HRP)-conjugated goat anti-rabbit secondary antibody (Abcam, UK) for 1 h. The immunoreactive signals were detected via a Western blotting detection system (V8, Tanon, China).

Calcium Influx Imaging: After the DRGs had adhered, the mature neuronal cells were cultured for 2–3 days and subsequently treated with PPy, and the PPyCA MVs were synthesized in vitro. The intracellular calcium ion levels of DRG cells were measured using a diluted Fluo-4 AM ester stock (4 μM). After the culture medium was removed, the cells were washed 3 times with PBS. Then, 500 μL of Fluo-4 AM ester solution was added to each well, and the cells were incubated with the DRGs at 37 °C for 30 min. Fluorescence images of the DRG cells were then acquired via CLSM (Leica TCS SP8). The excitation wavelength was 488 nm. A chemical stimulus, such as high KCl (100 mM), was applied, and the resulting calcium influx was recorded in video format. Images were analyzed offline with NIH ImageJ software or Leica Software. The data are presented as the relative change in fluorescence ($\Delta F/F_0$), where F_0 is the basal fluorescence and $\Delta F = F - F_0$.

In Vitro Synthesis of PPy/PPyCA: The polymerization of Py or PPyCA in the presence of CAT and H₂O₂ was monitored using a UV-vis spectrophotometer (Unico UV-4800, CN). A solution containing 5 mM Py or PPyCA, 1 mM H₂O₂, and 0.1 μM PSS was placed in a 1 cm quartz cell. Spectra were collected at ambient temperature at specified time intervals: 0 min, 10 min, 30 min, 90 min, 150 min, and 360 min.

Degradation of PPyCA: To investigate the degradation of PPyCA, 600 μg of PPyCA was dispersed in PBS at two different pH values, 7.4 and 6.5, each containing various concentrations of H₂O₂: 0.25, 0.5, and 1 mM.

Liquid Chromatography-Mass Spectrometry (LC-MS) Analysis: Degradation products were dissolved in nanopure water before LC-MS analysis by a liquid-mass analyzer (ORBITRAP FUSION LUMOS). An ACQUITY UPLC BEH C18 1.7 μm column (2.1 × 100 mm) was used in the chromatographic separation system. Chromatographic separation was conducted with a binary gradient of solvent A (water plus 0.1% formic acid) and solvent B (acetonitrile plus 0.1% formic acid) at a flow rate of 0.2 mL min⁻¹. The solvent gradient was applied for 43 min, 10–100% B, 0–5 min; 10–90% B, 5–40 min; and 90% B, 40–43 min.

Effects of Degradation Products on Cell Metabolism: The DRG oxygen consumption rate (OCR) was measured using a Seahorse XFe96 Extracellular Flux Analyzer (Seahorse Bioscience, Agilent) following the manufacturer's established protocols. Briefly, DRGs (3 × 10⁴) were seeded into 96-well XF cell culture microplates containing induction medium. On the day of the assay, the cells were treated with PPy or PPyCA degradation products (1 mM, pH 7.4) for 24 h, and then the medium was removed. The cells were then washed once with warmed assay medium (XF DMEM, pH 7.4, with 1 mM pyruvate, 2 mM glutamine, and 10 mM glucose) and incubated at 37 °C in a non-CO₂ incubator for 60 min. After incubation, the assay medium was replaced with fresh, warm medium, and oligomycin, FCCP, and rotenone/antimycin A were sequentially injected. The basal respiration, ATP-linked respiration, maximal respiration, and spare respiratory capacity were calculated using Wave Desktop 2.6 (Agilent Technologies), with the data normalized to the number of cells.

High-Resolution Untargeted Metabolomics: Following gradual thawing at 4 °C, an aliquot from each sample was introduced to a precooled mixture of methanol, acetonitrile, and water (2:2:1, v/v/v). The mixture was vortexed, subjected to low-temperature sonication for 30 min, incubated at 20 °C for 10 min, and then centrifuged at 14 000 ×g for 20 min at 4 °C. The supernatant was carefully collected and dried under a vacuum. For mass spectrometry analysis, 100 μL of acetonitrile/water mixture (1:1, v/v) was added to the dried sample, which was then vortexed and centrifuged at 14 000 ×g for 15 min at 4 °C. The resulting supernatant was used for injection and subsequent analysis. Chromatographic separation was achieved

via a Vanquish LC ultrahigh-performance liquid chromatography (UHPLC) system equipped with a hydrophilic interaction liquid chromatography (HILIC) column maintained at 25 °C with a flow rate of 0.3 mL min⁻¹ and an injection volume of 2 μL. The mobile phase comprised water with 25 mM ammonium acetate, 25 mM ammonia solution (A), and acetonitrile (B). The gradient elution program was structured as follows: from 0 to 1.5 min, 98% B; from 1.5 to 12 min, a linear decrease in B from 98% to 2%; from 12 to 14 min, B was constant at 2%; from 14 to 14.1 min, B linearly increased from 2% to 98%; and from 14.1 to 17 min, B was held at 98%. The samples were kept in an autosampler at 4 °C throughout the analysis. To counteract instrument signal fluctuations, samples were processed in a random order, and quality control (QC) samples were included intermittently to assess system stability and data reliability.

Following UHPLC separation, the samples were analyzed via electrospray ionization (ESI) via a Q Exactive series mass spectrometer (Thermo) in positive ionization mode. The ESI source settings were as follows: Gas 1 and Gas 2 at 60, curtain gas (CUR) at 30 psi, the ion source temperature at 600 °C, and the spray voltage (ISVF) at ± 5500 V. The first-level mass-to-charge (*m/z*) detection range was set from 80 to 1200 Da, with a resolution of 60 000 and a scan accumulation time of 100 ms. The second-level data-dependent acquisition method operated within a scanning range of 70 to 1200 Da, a resolution of 30 000, a scan accumulation time of 50 ms, and a dynamic exclusion time of 4 s.

The raw data were converted to mzXML format using ProteoWizard software, followed by peak alignment and retention time correction using XCMS software. The data extracted by XCMS were initially subjected to metabolite structural identification and data preprocessing. An experimental data quality assessment was subsequently performed, followed by data analysis.

Statistical Analysis: The data are presented as the standard error of the mean (mean ± SEM). Statistical analysis was performed via Excel, R, and Prism 9.02. For comparisons of treatment groups, two-tailed Student's *t*-test, one-way ANOVA, or two-way ANOVA was performed. Significance is denoted as follows: */#*P* < 0.05; **/##*P* < 0.01; ***/###*P* < 0.005; ****/####*P* < 0.001. The asterisk (*) indicates a comparison between the PPyCA and the control, whereas the hash (#) represents a comparison between the PPy group and the control. Details of the statistical analyses and “*n*” values can be found in the Figure Legends. For in vivo experiments, “*n*” indicates the number of rats.

Supporting Information

Supporting Information is available from the Wiley Online Library or from the author.

Acknowledgements

Y.Q., X.Q., and B.H. contributed equally to this work. This work was financially supported by the National Natural Science Foundation of China (22372196), the Key Projects of the National Natural Science Foundation of China (82230073), National Natural Science Foundation of Chongqing (CSTB2023NSCQ-MSX0419), and National Postdoctoral Researcher Support Program (GZC20233613).

Conflict of Interest

The authors declare no conflict of interest.

Data Availability Statement

The data that support the findings of this study are available from the corresponding author upon reasonable request.

Keywords

conductive polymers, degradable polymer, enzymatic synthesis, neural interface, π -conjugated polymers

Received: January 19, 2025

Revised: March 20, 2025

Published online:

- [1] a) J. Liu, N. Liu, Y. Xu, M. Wu, H. Zhang, Y. Wang, Y. Yan, A. Hill, R. Song, Z. Xu, M. Park, Y. Wu, J. L. Ciatti, J. Gu, H. Luan, Y. Zhang, T. Yang, H.-Y. Ahn, S. Li, W. Z. Ray, C. K. Franz, M. R. MacEwan, Y. Huang, C. W. Hammill, H. Wang, J. A. Rogers, *Science* **2024**, 383, 1096; b) V. A. Pavlov, K. J. Tracey, *Neuron* **2022**, 110, 3627; c) C. Pitsalidis, A. M. Pappa, A. J. Boys, Y. Fu, C. M. Moysidou, D. van Niekerk, J. Saez, A. Savva, D. Iandolo, R. M. Owens, *Chem. Rev.* **2022**, 122, 4700; d) X. Tang, H. Shen, S. Zhao, N. Li, J. Liu, *Nat. Electron.* **2023**, 6, 109.
- [2] a) Z. Liu, X. Wan, Z. L. Wang, L. Li, *Adv. Mater.* **2021**, 33, 2007429; b) E. Zeglio, A. L. Rutz, T. E. Winkler, G. G. Malliaras, A. Herland, *Adv. Mater.* **2019**, 31, 1806712.
- [3] a) M. Berggren, E. D. Glowacki, D. T. Simon, E. Stavrinidou, K. Tybrandt, *Chem. Rev.* **2022**, 122, 4826; b) A. Uva, S. Michailovich, N. S. Y. Hsu, H. Tran, *J. Am. Chem. Soc.* **2024**, 146, 12271.
- [4] a) J. Wu, J. Lin, P. Huang, *Chem. Soc. Rev.* **2023**, 52, 3973; b) D. T. Simon, E. O. Gabrielsson, K. Tybrandt, M. Berggren, *Chem. Rev.* **2016**, 116, 13009.
- [5] J. W. Salatino, K. A. Ludwig, T. D. Y. Kozai, E. K. Purcell, *Nat. Biomed. Eng.* **2017**, 1, 862.
- [6] B. Gupta, A. Saxena, M. L. Perillo, L. C. Wade-Kleyn, C. H. Thompson, E. K. Purcell, *Acc. Chem. Res.* **2024**, 57, 1346.
- [7] X. Strakosas, H. Biesmans, T. Abrahamsson, K. Hellman, M. S. Ejneby, M. J. Donahue, P. Ekstrom, F. Ek, M. Savvakis, M. Hjort, D. Bliman, M. Linares, C. Lindholm, E. Stavrinidou, J. Y. Gerasimov, D. T. Simon, R. Olsson, M. Berggren, *Science* **2023**, 379, 795.
- [8] I. B. Dimov, M. Moser, G. G. Malliaras, I. McCulloch, *Chem. Rev.* **2022**, 122, 4356.
- [9] T. Nezakati, A. Seifalian, A. Tan, A. M. Seifalian, *Chem. Rev.* **2018**, 118, 6766.
- [10] a) J. Liu, Y. S. Kim, C. E. Richardson, A. Tom, C. Ramakrishnan, F. Birey, T. Katsumata, S. Chen, C. Wang, X. Wang, L. M. Joubert, Y. Jiang, H. Wang, L. E. Fenno, J. B. Tok, S. P. Pasca, K. Shen, Z. Bao, K. Deisseroth, *Science* **2020**, 367, 1372; b) C. D. Sessler, Y. Zhou, W. Wang, N. D. Hartley, Z. Fu, D. Graykowski, M. Sheng, X. Wang, J. Liu, *Sci. Adv.* **2022**, 8, ade1136; c) A. Zhang, Y. Jiang, K. Y. Loh, Z. Bao, K. Deisseroth, *Nat. Rev. Bioeng.* **2023**, 2, 82; d) B. W. Walker, R. P. Lara, E. Mogadam, C. H. Yu, W. Kimball, N. Annabi, *Prog. Polym. Sci.* **2019**, 92, 135.
- [11] a) A. Mariano, C. Lubrano, U. Bruno, C. Ausilio, N. B. Dinger, F. Santoro, *Chem. Rev.* **2021**, 122, 4552; b) F. Amorini, I. Zironi, M. Marzocchi, I. Gualandi, M. Calienni, T. Cramer, B. Fraboni, G. Castellani, *ACS Appl. Mater. Interfaces* **2017**, 9, 6679.
- [12] Y. Qin, Y. Fan, R. Chen, H. Yin, H. Zou, X. Qu, J. Tan, Y. Xu, C. Zhu, *Nano Lett.* **2022**, 22, 3825.
- [13] a) M. Mittal, M. R. Siddiqui, K. Tran, S. P. Reddy, A. B. Malik, *Antioxid. Redox Signal* **2014**, 20, 1126; b) E.-M. Krämer-Albers, *Nat. Cell Biol.* **2018**, 20, 225.
- [14] G. Bodega, M. Alique, L. Puebla, J. Carracedo, R. M. Ramirez, *J. Extracell Vesicles* **2019**, 8, 1626654.
- [15] a) B. Guo, L. Glavas, A.-C. Albertsson, *Prog. Polym. Sci.* **2013**, 38, 1263; b) S. Jadoun, U. Riaz, V. Budhiraja, *Med. Devices Sens.* **2020**, 4, 10141; c) Y. Dai, S. Wai, P. Li, N. Shan, Z. Cao, Y. Li, Y. Wang, Y. Liu, W. Liu, K. Tang, Y. Liu, M. Hua, S. Li, N. Li, S. Chatterji, H. C. Fry, S. Lee, C. Zhang, M. Weires, S. Sutyak, J. Shi, C. Zhu, J. Xu, X. Gu, B. Tian, S. Wang, *Science* **2024**, 386, 431.
- [16] M. L. Petrus, R. K. M. Bouwer, U. Lafont, D. H. K. Murthy, R. J. P. Kist, M. L. Böhm, Y. Olivier, T. J. Savenije, L. D. A. Siebbeles, N. C. Greenham, T. J. Dingemans, *Polym. Chem.* **2013**, 4, 4182.
- [17] a) M. Mohammed, L. P. Mekala, S. Chintalapati, V. R. Chintalapati, *J. Hazard. Mater.* **2020**, 385, 2105416; b) P. Humpolicek, V. Kasparkova, J. Pachernik, J. Stejskal, P. Bober, Z. Capakova, K. A. Radaszkiewicz, I. Junkar, M. Lehocky, *Mater. Sci. Eng. C Mater. Biol. Appl.* **2018**, 91, 303.
- [18] H. Jin, K. Kim, S. Park, J. Rhee, H. Ahn, D. J. Kim, K. Kim, J. H. Noh, T. S. Kim, E. Y. Shin, H. J. Son, *Adv. Funct. Mater.* **2023**, 33, 2304930.
- [19] Y. C. Woo, S. S. Park, A. R. Subieta, T. J. Brennan, *Anesthesiology* **2004**, 101, 468.
- [20] a) R. B. Said, J. M. Kollé, K. Essalah, B. Tangour, A. Sayari, *ACS Omega* **2020**, 5, 26125; b) A. V. Artiukhov, A. Grabarska, E. Gumbarewicz, V. A. Aleshin, T. Kähne, T. Obata, A. V. Kazantsev, N. V. Lukashev, A. Stepulak, A. R. Fernie, V. I. Bunik, *Sci. Report.* **2020**, 10, 1886; c) P. Ma, Y. S. Deshmukh, C. H. R. M. Wilsens, M. Ryan Hansen, R. Graf, S. Rastogi, *Sci. Report.* **2015**, 5, 13280; d) M. M. Tawfik, K. T. Yamato, T. Kohchi, T. Koeduka, K. Matsui, *Biosci. Biotechnol. Biochem.* **2017**, 81, 1148.
- [21] V. Varade, G. V. Honnavar, P. Anjaneyulu, K. P. Ramesh, R. Menon, *J. Phys. D: Appl. Phys.* **2013**, 46, 365306.
- [22] B. Dimitris, R. Garg, E. Angelopoulos, D. K. Cullen, F. Vitale, *Nat. Commun.* **2025**, 16, 1861.
- [23] C. Wang, Y. Liu, X. Qu, B. Shi, Q. Zheng, X. Lin, S. Chao, C. Wang, J. Zhou, Y. Sun, G. Mao, Z. Li, *Adv. Mater.* **2022**, 34, 121571.
- [24] H. Nakanishi, H. Obaishi, A. Satoh, M. Wada, K. Mandai, K. Satoh, H. Nishioka, Y. Matsuura, A. Mizoguchi, Y. Takai, *J. Cell Biol.* **1997**, 139, 951.
- [25] B. L. Chen, L. J. Wang, X. J. Li, Z. Shi, J. Duan, J. A. Wei, C. Z. Li, C. Q. Pang, D. Y. Wang, K. J. Zhang, H. Chen, W. Y. Na, L. Zhang, K. F. So, L. B. Zhou, B. Jiang, T. F. Yuan, Y. B. Qu, *Mol. Psychiatry* **2022**, 29, 1583.
- [26] M. Estacion, B. P. S. Vohra, S. Liu, J. Hoeijmakers, C. G. Faber, I. S. J. Merkies, G. Lauria, J. A. Black, S. G. Waxman, *J. Neurophysiol.* **2015**, 114, 1554.
- [27] O. Nikolaienko, S. Patil, M. S. Eriksen, C. R. Bramham, *Semin. Cell Dev. Biol.* **2018**, 77, 33.